crystals

MDPI

Article

2D Organic–Inorganic Halide Perovskites for Hybrid Heterostructures: Single Crystals, Thin Films and Exfoliated Flakes

Fabrizio Ciccarelli [1], Mario Barra [1], Antonio Carella [2], Gabriella Maria De Luca [3], Felice Gesuele [3] and Fabio Chiarella [1,*]

[1] CNR-SPIN, c/o Dipartimento di Fisica "Ettore Pancini", P.le Tecchio, 80, I-80125 Napoli, Italy; fabrizio.cclls@gmail.com (F.C.); mario.barra@spin.cnr.it (M.B.)
[2] Dipartimento di Scienze Chimiche, Università degli Studi di Napoli 'Federico II', Complesso Universitario Monte Sant'Angelo, Via Cintia 21, I-80126 Napoli, Italy; antonio.carella@unina.it
[3] Dipartimento di Fisica 'E. Pancini', Università degli Studi di Napoli 'Federico II', Complesso Universitario Monte Sant'Angelo, Via Cintia 21, I-80126 Napoli, Italy; gabriellamaria.deluca@unina.it (G.M.D.L.); felice.gesuele@unina.it (F.G.)
* Correspondence: fabio.chiarella@spin.cnr.it

Abstract

Rapid progress on the fabrication of lead halide perovskite has led to the development of high performance optoelectronic devices, particularly in the field of solar cell technologies. This initial success has subsequently inspired investigations into layered 2D-halide perovskite structures, motivated in part by their good environmental stability, but more significantly by their intriguing fundamental photo-physics. They have recently been used to improve the photoresponsivity of monolayer transition metal dichalcogenides in hybrid heterostructures. In this paper, we report on the synthesis of the $(PEA)_2(MA)_{n-1}Pb_nI_{3n+1}$ series (with $n = 1, 2, 3$) of 2D-halide perovskites, in order to develop a platform that provides ultra-thin layers for the fabrication of hybrid heterostructures. The crystal synthesis method and its basic structural and optical characterization are shown, highlighting the differences in the crystal synthesis processes. Furthermore, we explore the preparation of 2D halide perovskite ultra-thin flakes using the mechanical exfoliation method, and few-layer-areas of $n = 1$ member of the series are identified using atomic force microscopy. Finally, we study the deposition of thin and ultra-thin films using the spin coating technique to provide an alternative process to the exfoliation.

Keywords: halide perovskite; single crystals; 2D materials; thin films

Academic Editor: Sawanta Mali

Received: 24 October 2025
Revised: 18 November 2025
Accepted: 26 November 2025
Published: 29 November 2025

Citation: Ciccarelli, F.; Barra, M.; Carella, A.; De Luca, G.M.; Gesuele, F.; Chiarella, F. 2D Organic–Inorganic Halide Perovskites for Hybrid Heterostructures: Single Crystals, Thin Films and Exfoliated Flakes. *Crystals* **2025**, *15*, 1024. https://doi.org/10.3390/cryst15121024

1. Introduction

Hybrid halide perovskites are an increasingly investigated set of semiconductors that are very attractive and fascinating, owing to their outstanding optical and electronic properties. This semiconductor class has a direct bandgap with a high optical absorption coefficient [1] and a long charge carrier lifetime [2]. The main uses of hybrid halide perovskites are in solar cells [3], but there is an increasing interest in their application in other electronic and optoelectronic devices, such as thin-film transistors [4], memristors [5], phototransistors and photodetectors [6], light emitting diodes [7], and lasing [8].

These materials are "hybrid" in the sense of the contemporary presence of organic and inorganic elements in their chemical composition, and are categorized in two families called 2D (or quasi-2D) and 3D perovskites. The 3D hybrid perovskites are characterized

by a pseudo-cubic structure with the formula ABX_3 where A is a small organic cation that can be either methylammonium (MA) or formamidinium (FA), B is an inorganic cation (mainly lead or tin), and X is a halogen atom, all connected by covalent and ionic bonds. The best known example of this family is the MAPI compound (methylammonium lead iodide, formula $(CH_3NH_3)PbI_3$), which demonstrated astonishing performances when employed in photovoltaic devices [9]. The structure of 2D and quasi-2D hybrid halide perovskites (2D-PVKs) differs significantly from their 3D counterparts due to the presence of an organic cation layer, which cuts through the perovskite structure and provides a layered-sheet-like arrangement (see the sketch in Figure 1). The general formula changes to $(R{-}NH_3)_2(A)_{n-1}B_nX_{3n-1}$, where R is an organic radical and n indexes the thickness of the perovskite layers sandwiched between two organic layers. This forms a Ruddlesden–Popper-like phase [10], where the 3D structure can be seen as the limit of the series with the n-index, which tends to infinity.

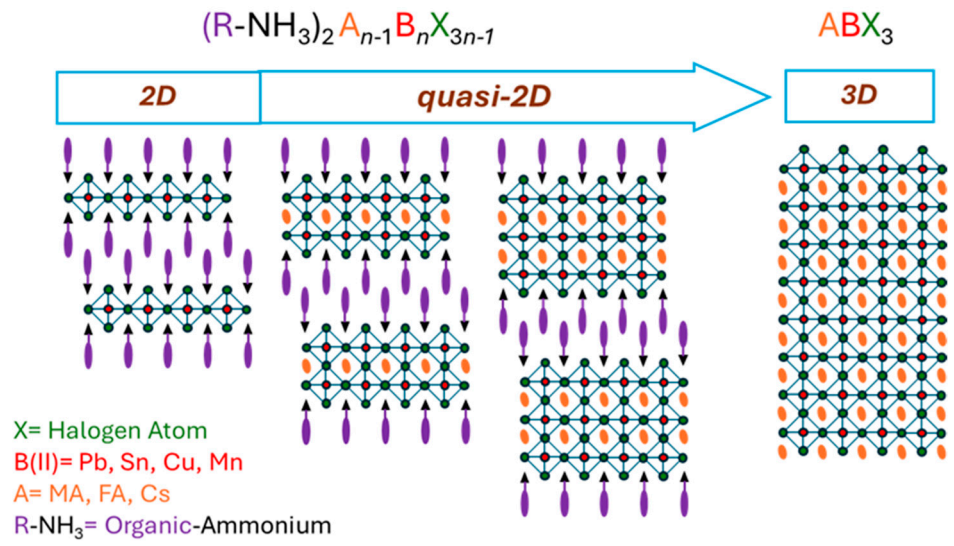

Figure 1. Sketch of the 2D-PVK Ruddlesden–Popper series structure after increasing the n index from 1 to 3, in comparison with the 3D-PVKs structure.

Charge transport and optoelectronic properties in 2D-PVKs are confined within the inorganic layers. However, the organic radicals R (typically butylammonium BA or phenethylammonium PEA) are bonded via van der Waals interactions, giving rise, in one direction, to a stack of multiple layers with reduced interlayer interactions that enable exfoliation of ultra-thin layers. Therefore, 2D-PVKs could also be classified as "2D-materials". Unlike commonly used organic spacers such as butylammonium (BA) or octylammonium (OA), phenethylammonium (PEA) offers advantages such as well-defined layer spacing, stronger framework stabilization, and reduced structural disorder via π–π interactions, as well as enhanced dielectric and quantum confinement due to the more polarizable aromatic structure and higher dielectric constant compared with the long-chain aliphatic spacers. On the other hand, the π–π interactions introduced by the choice of PEA could make the mechanical exfoliation process of the crystals more complex. Due to the hydrophobic barrier formed by the organic cation layers encapsulating the inorganic layers, 2D-PVKs exhibit better moisture stability under ambient conditions with respect to 3D perovskites. Furthermore, the intercalated organic–inorganic layers form a natural multi-quantum-well structure with dielectric confinement [11]. They show very high oscillator strength and remarkably large (~500 meV) binding energies (in particular for lead-based compounds [12]), long lifetime, and long diffusion length of the exciton [13]. These optoelectronic properties are tunable

by adjusting the number of perovskite inorganic layers (n in the formula), and increasing n (more stacking) leads to properties closer to that of the corresponding 3D-phase.

In recent years, there has been considerable interest in 2D-PVKs as promising materials in low-cost, high-performance optoelectronic devices [14], and a wide range of controllable process are available to lay down single crystals [15,16] as well as thin film fabrication methods such as spin coating [17], blade coating [18], co-evaporation in vacuum [19,20], and single source thermal ablation [21]. It has also been demonstrated that these van der Waals crystals can be exfoliated to produce atomically thin, large, stable, and homogeneous sheets with interesting optical properties [22,23]. Besides the intrinsic interest in these novel 2D systems, they represent a unique new building block for the construction of hetero-structured systems [24] due to the possibility of modulating their optoelectronic properties with chemical substitution in the halogen site, the metal, the A cation site, and the organic amine [10,25].

Recently, several studies on heterostructures composed with 2D-PVKs and transition-metal dichalcogenides (TMDs) have been reported, showing excellent interlayer exciton formation [26], enhancement of photoluminescent emission [27], and photodetection [28,29]. These van der Waals structures show type II level alignment [23,30] with electron hole separation. The application of 2D-PVK based photodetectors is limited to the visible region of the light spectra because of their large bandgap, while the combination of a few layers of 2D-PVKs and monolayers of TMDs can lead to the formation of an interlayer gap lower than 1 eV, and, consequently, to efficient near-infrared detection.

In this framework, the object of this work consisted of the realization of an ultra-thin layer of 2D-PVKs with raw formula $(PEA)_2(MA)_{n-1}Pb_nI_{3n+1}$ (with n = 1, 2, 3, PEA = $C_6H_5C_2H_4NH_3$ and MA = CH_3NH_3) in preparation for staking with TMDs monolayers to form hybrid heterostructures via mechanical exfoliation of single crystals, and, as an alternative approach, we investigate the feasibility of producing ultra-thin films through the spin coating technique. In this work, our approach was to provide a reliable source of ultra-thin layers via mechanical exfoliation or spin coating, suitable for the realization of hybrid heterostructures with improved interfacial properties. For this task, the bulk contribution must be reduced to avoid interposing and/or interfering with the interfacial state.

Although the mechanical exfoliation process is very effective and cheap, it requires a supply of large, pure crystals, and process scalability and reproducibility are required. The study of crystal growth is mandatory to accomplish the fabrication task of hybrid heterostructures using mechanical exfoliation and the mechanical transfer method, as already widely experienced with TMD semiconductors.

On the other hand, the synthesis of 2D-PVKs single crystals with $n > 1$ is a challenging task for several reasons. Controlling the crystallization phase requires careful consideration of multiple parameters, including crystallization kinetics (organic and inorganic layers exhibit different growth rates), solubility and chemical interactions (large cations, R–NH_3, have limited solubility and interact less favorably with PbI_2 compared to smaller cations, A, leading to segregation), and thermodynamic stability (low-n phases are less stable with respect to the n = 1 and the three-dimensional ($n \to \infty$) phases, which complicates both synthesis and long-term preservation).

Furthermore, the study and understanding of crystallization processes are fundamental to better understanding the processes of thin film formation with solution-based techniques such as spin coating.

2. Crystal Growth and Characterization

2.1. Starting Materials

The precursors of the crystals that were used are: phenetylammonium iodide, (PEAI) lead iodide (PbI_2), and methylammonium iodide (CH_3NH_3I) salts (MAI), all provided by Merck (eu), and lead(II) oxide (PbO), bought from Carlo Erba (it). These reagents were used without further purification. The solvents that were used are: hydriodic acid (HI (55–58%)) purchased from Alfa Aesar (uk), ethylene glycol, and diethyl ether from Merck.

2.2. Synthesis

In this work, we focus on the synthesis of single crystals in the member with n = 1, 2, 3 of the lead-based hybrid halide perovskites family, i.e., $(PEA)_2PbI_4$, $(PEA)_2(MA)Pb_2I_7$ and $(PEA)_2(MA)_2Pb_3I_{10}$, abbreviated as PEPI-1, PEPI-2, and PEPI-3, respectively The crystallization procedures for all the compounds are detailed below and illustrated in the summary diagram of Figure 2.

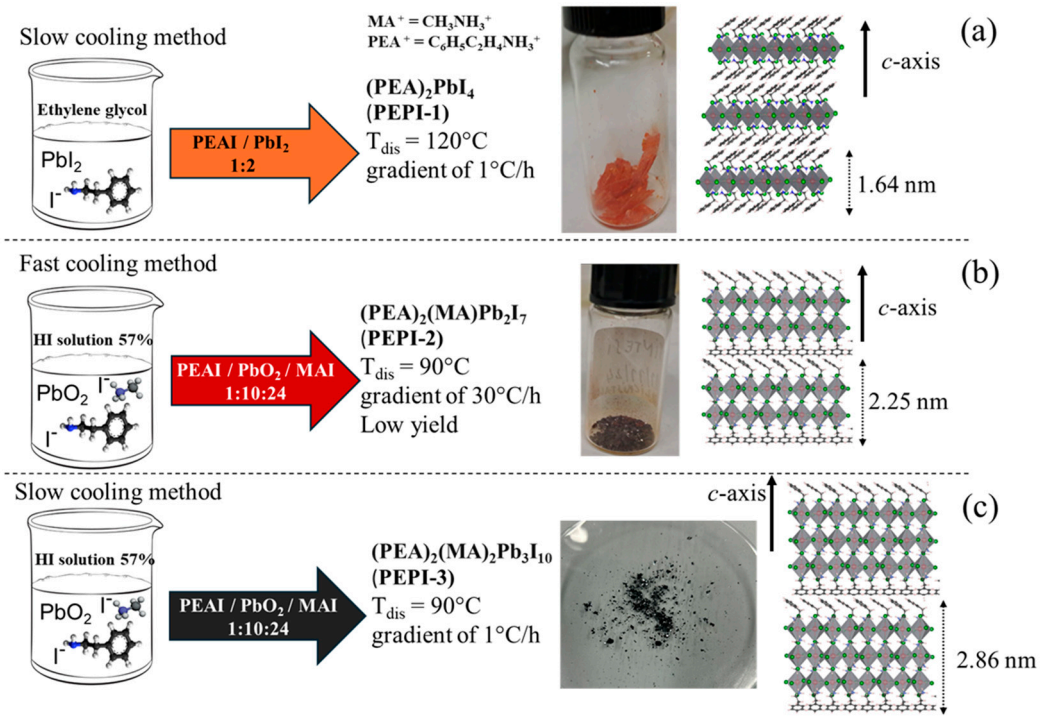

Figure 2. Summary diagram of the crystallization procedures followed for the compounds PEPI-1 (**a**), PEPI-2 (**b**), and PEPI-3 (**c**) (from top to bottom). From left to right, we summarize the synthesis method, the precursor molar ratio (within the arrows), the crystallization parameters (T_{dis} is the dissolution temperature), a photograph of the collecting crystals, and the sketch of the crystal structure oriented along the *c*-axis with the estimated thickness of the relative monolayers.

PEPI-1: The n = 1 member of the series was synthesized via a temperature-lowering method. The reagents were dissolved in ethylene glycol in a vial, according to the stoichiometric ratio (in PEPI-1 compound, PbI_2 and PEAI are in 1:2 molar ratio). The vial was heated up to T = 120 °C on a hot stirring plate until total dissolution. Subsequently, a slow cooling was carried out in the oven with a gradient of 1 °C/h until room temperature was reached. At the end, the solution was filtered, and the crystals were recovered and washed with diethyl ether. Orange platelet-shape crystals are obtained (see Figure 2a) with a size in the scale of millimeters and a yield of around 90%.

PEPI-2: we synthesize n = 2 member of the series using a slightly modified procedure previously reported in the literature [31], which consists of a temperature lowering method

with a very slow cooling ramp. The precursors are PbO, MAI and PEAI. The molar ratio between them is 10:24:1. This does not follow the stoichiometry of the crystal, which should be 3:2:2. A total of 0.33 mmol of PbO, 0.80 mmol of MAI, and 0.033 mmol of PEAI are dissolved in the HI solution (55–58% w/w) at 90 °C until total dissolution. The set temperature on the hot stirring plate decreases with a faster cooling ramp of 0.5 °C/min until room temperature is reached, then the vial is put aside to make the crystal grow. Many crystals of a few hundred microns were obtained with a dark-red color (see Figure 2b). The total mass is 0.020 g with a yield of 62%.

PEPI-3: the n = 2 member of the series was synthesized following a protocol similar to that employed for PEPI-2, as discussed above. The basic differences are related to the increase by a ratio of five times the mass of the precursors and by a change of 1 °C/h in the cooling ramp in the oven. After five days, with the oven at room temperature, the vial was checked, and no crystal was formed yet. Then, the walls of the vial were touched slightly to create sites of nucleation. After five hours, the growth of dark grey flakes was observed (see Figure 2c), which were finally recovered with the usual washing step. A total of 20 mg of crystals were obtained, with a yield of 9.2%.

2.3. X-Ray Characterization

Single crystals were characterized by X-ray diffraction (XRD) in Brag–Brentano configuration to check the crystal structure and the presence of spurious phases. In the case of the PEPI-1 compound, we performed the analysis on a single crystal because the crystal size is greater than the x-ray beam spot (Ø 2 mm). Conversely, in the cases of the PEPI-2 and PEPI-3 compounds, the crystals obtained in each crystallization were casually dispersed on a glass support covered with a thin layer of grease (Apiezon M, M&I Materials Ltd., Manchester, UK), working as a glow, and then placed directly under the X-ray beam.

PEPI-1: the XRD spectra of a single crystal are plotted in Figure 3a. One peak at 5.29° is measured with its replicas corresponding to the (0 0 2ℓ) planes diffraction peaks, because the c-axis of the crystal is perpendicular to the substrate. This is an indication of the formation of the PEPI-1 phase, as reported in [31]. This corresponds to a c-axis spacing of about 3.274 ± 0.001 nm, close to the value reported in the literature on single crystals [32], and, consequently, to a nominal value of a monolayer thickness of 1.64 nm (see sketch in Figure 2). No peaks related to the reagent phases were observed.

PEPI-2: from the XRD spectra reported in Figure 3b, we observe the diffraction peaks related to the (0 0 2ℓ) planes. All the crystals, formed with a sheet-like shape, tend to land on the glass support with the c-axis perpendicular to the support surface (see sketch in Figure 2). As also discussed in [31], this indicates the presence of a crystalline PEPI-2 with intense peaks. We observe a peak at 3.93° that is characteristic of the PEPI-2 compound. This corresponds to a c-axis of about 4.506 ± 0.008 nm and to a monolayer of about 2.25 nm. Although no trace of PEPI-1 and PEPI-3 was visible, we observe a spurious peak at 14.10°, indicating the presence of MAPI crystals in the collection [33].

PEPI-3: Figure 3c shows the XRD spectra with a peak at 3.11° and its replicas, consistent with a c-axis of approximatively 5.716 ± 0.016 nm and to a monolayer of 2.86 nm. No peak of PEPI-1, PEPI-2, or MAPI was found.

As a whole, the reported values of the c-axis for the three compounds are consistent with the results discussed in [31], and it is possible to calculate an increase of approximately 0.61 nm in the monolayer thickness for each increment in the n index of the compound structure.

It is worth noting that the gradient of the temperature significantly affects the composition of the crystals. Indeed, during the synthesis of PEPI-2 and PEPI-3, the cooling ramp was the only different parameter, while the stoichiometric ratio and the dissolving temperature were kept fixed.

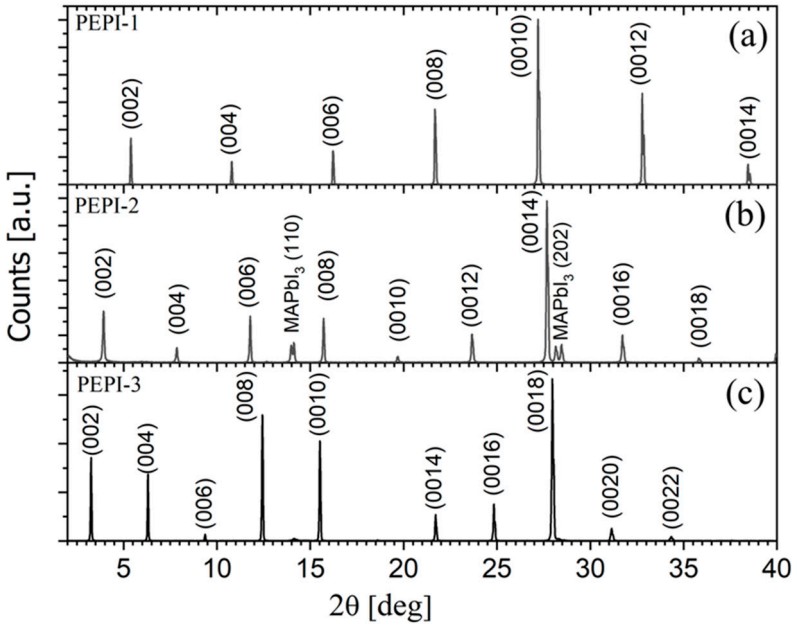

Figure 3. X-ray diffractogram of PEPI-1 (**a**), PEPI-2 (**b**), and PEPI-3 (**c**). All the spectra were acquired with a Rigaku diffractometer using a Cu Kα1 (λ = 1.5406 Å) source, a step size of 0.01°, and a speed of 0.5 s/step. The acronym MAPI indicates the phase of the $(CH_3NH_3)PbI_3$ compound.

2.4. Optical Characterization

To correlate structure and composition with the steady-state optical response of the PEPI-1, PEPI-2, and PEPI-3 single crystals, photoluminescence (PL) spectroscopy measurements were performed using a scanning confocal optical microscope operating in epi-illumination configuration [34]. In Figure 4a, a portion of the optical micro-PL setup used for the measurements is shown, outlining the excitation and collection geometry. The excitation source was a 450 nm continuous-wave laser (NPL45B, Thorlabs, Newton, NJ, USA), whose collimated output was focused onto the sample through a 10× microscope objective (numerical aperture 0.25). This objective was selected as an optimal compromise between spatial resolution, estimated to be approximately 1 micron, and the long working distance required by the thickness of the investigated crystals.

The backscattered PL signal emitted from the sample was collected by the same objective and directed to the detection arm of the setup. The emission was filtered using two high-quality long-pass filters to efficiently suppress the excitation light and then coupled into a 100 µm-core optical fiber, which also acted as a confocal pinhole to ensure spatial selectivity. The collected light was analysed by a 320 mm focal-length spectrometer (iHR320, Horiba, Kyoto, Japan) equipped with a thermoelectrically cooled, back-illuminated CCD detector. The excitation power was maintained below 1 mW at the sample plane to prevent any photoinduced degradation or local heating effects.

The PL spectra of the three phases of Ruddlesden–Popper (RP) perovskite crystals are displayed in Figure 4b. The data reveal a clear evolution of the emission energy with the number of inorganic layers (n), showing well-defined peaks at 531.1 ± 0.2 nm (PEPI-1), 579.3 ± 0.4 nm (PEPI-2), and 625.3 ± 0.4 nm (PEPI-3); the error was estimated from a statistic made on various spectra acquired at different positions. These values correspond to emission energies of approximately 2.33, 2.14, and 1.98 eV, respectively, consistent with the expected reduction of quantum and dielectric confinement as n increases [35,36].

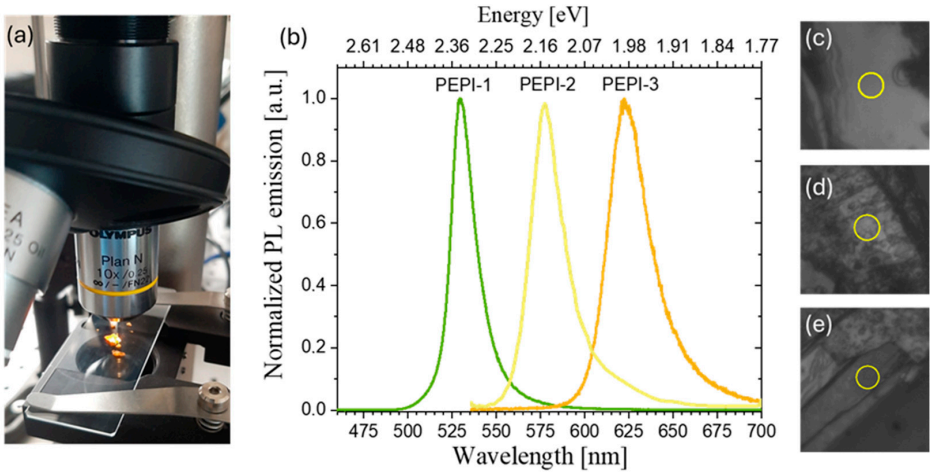

Figure 4. (**a**) Detail of the confocal micro-PL setup, operating in epi-illumination mode, illustrating the excitation and collection of optical paths. (**b**) Photoluminescence (PL) spectra of Ruddlesden–Popper perovskite crystals with different numbers of inorganic layers (n = 1, 2, 3), showing distinct excitonic emission peaks at 2.33, 2.14, and 1.98 eV as reported in the inset graph. (**c**–**e**) Optical micrographs of representative PEPI-1, PEPI-2, and PEPI-3 crystals, respectively, each marked with the location of the PL collection area (yellow circles) with a diameter of about 1 μm.

Panels (c), (d), and (e) in Figure 4 present optical micrographs of the investigated regions of PEPI-1, PEPI-2, and PEPI-3 crystals, respectively, each marked with the specific area from which the PL signal was collected, highlighting the spatial selectivity and reproducibility of the measurements. We verified that all PL measurements were performed in the linear excitation regime, where the emitted PL intensity scales proportionally with excitation power, and the spectral shape and peak position remain unchanged, ensuring that the reported spectra reflect the intrinsic emission of the crystals; i.e., they are not affected by saturation or heating effects.

The structural (XRD) characterization, together with the expected PL redshift from n = 1 to n = 3 due to reduced quantum confinement, confirms the successful fabrication of well-defined RP phases. We also have acquired and compared spectra at multiple positions across each single crystal or analysed flakes. All spectra exhibit the same peak position and line shape, confirming the homogeneity of the films. A detailed investigation of the emission dynamics, however, requires time-resolved PL measurements that are beyond the scope of this fabrication-focused study and will be addressed in future work. Our measurements enable localized excitation and spatially resolved analysis of single-crystal regions. Within the spatial resolution of our setup, the PL spectra exhibit sharp, intense peaks and minimal inhomogeneous broadening, confirming the high optical quality and phase purity of the synthesized perovskite domains.

Spatially resolved spectra of the PEPI-2 phase show the occasional occurrence of a weak additional emission feature around 730 nm (see Figure S1 in Supplementary Materials), which is likely associated with the formation of residual inclusions or intercalated regions on the crystal surface. Typically, the emission of MAPI occurs at around 775 nm, while an emission at 730 nm can be associated with a higher member of the RP series [36,37]. This is not associated with what was observed in the XRD analysis of the PEPI-2 crystal collection (see Figure 3b), which is related to the presence of bulk MAPI crystals intermingled with those of PEPI-2. In contrast, for the samples of PEPI-1 and PEPI-3, spatially resolved spectra do not show significant variations from the representative PL spectra reported in the literature, indicating excellent uniformity and structural homogeneity across the probed crystal areas.

3. Exfoliated Flakes and Ultra-Thin Films

The second part of this work focused on the fabrication of ultra-thin 2D-PVKs layers suitable for integration into heterostructures. We tested two different approaches: mechanical exfoliation of single crystals and spin coating technique.

3.1. Mechanically Exfoliated Flakes

This approach allows van der Waals 2D materials to be prepared in ultra-thin single crystal flakes (in the order of a monolayer or a few layers). This technique offers the key advantage of producing high-quality samples in terms of both crystalline quality and surface homogeneity. These features have been crucial for fundamental research and have led to the discovery of new phenomena, as well as, from technological point of view, giving the possibility of easily fabricating testing field-effect transistors and photodetectors demonstrating the practical applications of 2D materials in electronics and optoelectronics [24]. Therefore, we apply a mechanical exfoliation method to the 2D-PVK crystals to avoid flakes composed of just few crystalline layers. In this context, the fabrication of monolayers for optoelectronic applications is a mandatory requirement for TMDs, as they exhibit a direct band gap only when reduced to molecular thickness [38], whereas this constraint is less stringent for 2D-PVKs. Unlike TMDs, indeed, 2D-PVK semiconductors are direct-gap materials independent of the crystal thickness, and the nature and magnitude of the energy gap do not vary with it.

Few-layer thin flakes were peeled off from a PEPI-1 crystal platelet 11 $\times$ 3 mm^2 in size, as synthesized (see Figure 5a), using a Scotch tape micromechanical cleavage technique. The crystals were attached to a glass substrate with double-sided tape and then exfoliated using the tip of a blade to pry the crystal edge, and transferred onto a 200 nm SiO_2 layer covering a heavily doped Si substrate. An AFM image of a triangular flake 5 $\times$ 5 µm^2 in size is reported in Figure 5b. In this case, we measure along a profile of a thickness of 8.3 $\pm$ 0.5 nm. Assuming, as reported in [31,39] and confirmed by the XRD analysis, that the height of a monolayer is about 1.64 nm, the thickness value would correspond to a sample five layers thick. In the case of PEPI-2 and PEPI-3, on the other hand, the exfoliation via the Scotch tape cleaving process was found to produce very small flakes (one hundred nanometers) which proved to be unusable for our purposes, e.g., to create phototransistors.

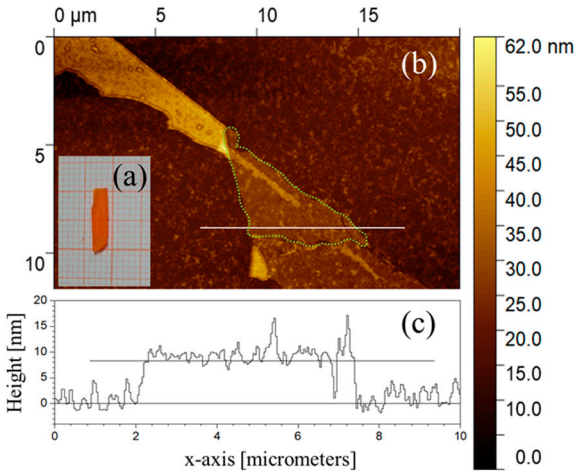

Figure 5. (**a**) Photograph of a PEPI-1 crystal on graph paper (minimum distance between line marks is 1 mm) used for the exfoliation process; (**b**) AFM image acquired by XE-100 from Park System in true non-contact mode using a ppp-NCHR tip by Nanosensors^{TM} (Neuchatel, Switzerland). The green dotted line is a guide for the eyes indicating the flake under consideration. (**c**) In the bottom part of the image, the data of a profile corresponding to the white line on the AFM image is plotted. On the right is positioned a color gradient bar as a reference for the heights.

3.2. Spin Coating Thin and Ultra-Thin Films

The deposition of thin films using the spin coating technique was tested parallel to the flake exfoliation study.

To realize PEPI-1 polycrystalline thin films, we dissolved precursor salts in stoichiometric ratio (PbI_2:PEAI = 1:2) in N,N-dimethylformamide (DMF) solvent by Merck, and stirred them at room temperature for 10 min. A volume of 20 µL of the resulting solution was taken using a Gilson pipette and was spread by a spin coater (model Laurell WS-650L, Laurell Technologies Corporation, Lansdale, PA, USA) on *n*-type highly doped silicon substrates (thickness of 500 µm) terminated with 200-nm-thick thermally-growth silicon dioxide (SiO_2). We varied the deposition parameters (solution molar concentration and spinning speed) to optimize the quality of the crystal phase and surface morphology, and to control the film thickness. We changed the concentration from 0.05 M to 1.5 M and the spinning speed from 2000 to 6000 rpm, while acceleration and spinning time were fixed at 1500 rad/s^2 and 60 s, respectively. No significant effect on film formation was observed by changing the spinning speed, which was finally set at 3000 rpm. After the coating procedure, all the samples were annealed at 100 °C for 10 min on a hot plate to improve the solvent desorption, increase the island dimension, and improve the structural order as discussed in [40], and were stored in nitrogen atmosphere to prevent degradation. To validate this procedure, in Figure 6a the XRD spectra of films deposited in the same conditions but with and without the post-annealing process are plotted. The XRD spectra show narrow and sharp peaks, which are a signature of high-quality perovskite films. Otherwise, in the as-grown films, we observed the presence of unreacted PEAI phase that disappears after the post-deposition annealing procedure. This effect was also visible in the absorption measurement reported in Figure 6b. The peak at 365 nm is typical of the formation of PbI_4^- [41,42] and is probably due to the presence of unreacted PEAI, an effect that strongly decreases after the annealing process.

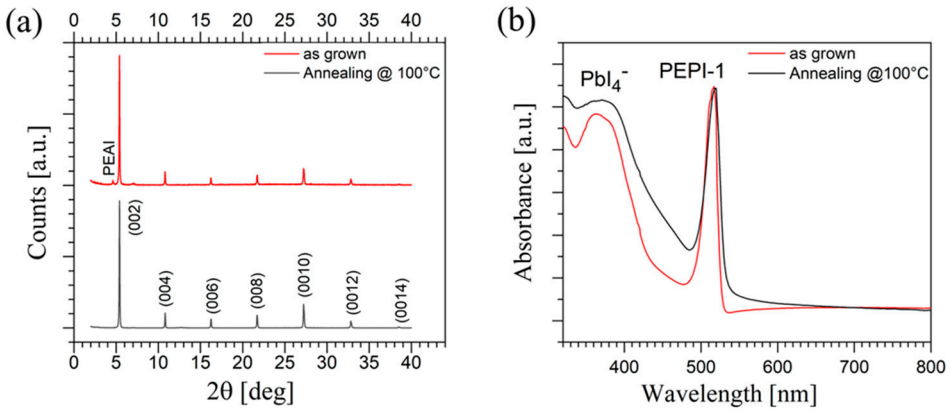

Figure 6. (**a**) XRD and (**b**) optical absorption spectra of an as-grown $(C_6H_5C_2H_4)_2PbI_4$ (PEPI-1) film (red lines) and of the same film after the annealing process (black curves). Optical spectra were acquired with a Jasco V-730 spectrophotometer (JASCO Corporation, Tokyo, Japan) in transmittance mode (except in this case, the measurements were performed on films prepared on a glass substrate).

We tried to achieve films for PEPI-2 and PEPI-3 compounds with a similar procedure. In all our attempts, starting from stoichiometric or non-stoichiometric molar ratios and/or using hot or cold solutions, pure-phase films could not be obtained. Films with multiple phases and with MAPI formed as observed in XRD. The absorption spectra are in Figure S2 in Supplementary Materials. As suggested by the crystal synthesis process, the transition from PEPI-2 to PEPI-3 formation is simply influenced by the cooling temperature gradient of the solution. Therefore, in our spin coating process, we tried heating the stoichiometric

and un-stoichiometric solution at 100 °C, but the process was too fast, and, above all, the concentration changed quickly during the process (lasting a few seconds). This inevitably led to the formation of all the phases. In this case, the post-annealing procedure did not provide positive feedback on the correct formation of the phase.

Atomic force microscopy (AFM) was used to characterize the morphology of the deposited films (see Figure 7a–d) and to estimate their thickness. In this way, we analysed the relation between the film thickness and the molar concentration used in the precursor solution, obtaining a linear relation (shown in Figure S3 in Supplementary Materials) with a slope of 0.75 μm/M. AFM images show compact and homogeneous coatings with the formation of cracks when the film thickness exceeds 80 nm. In all the films, we observed the presence of lamellar crystallites, which became increasingly sparse and smaller as the film thickness decreased. For the thinner film (around 12 nm), the surface appeared to be formed of small connected islands of a diameter of about a few hundred nm. Below this thickness, discontinuous films were obtained.

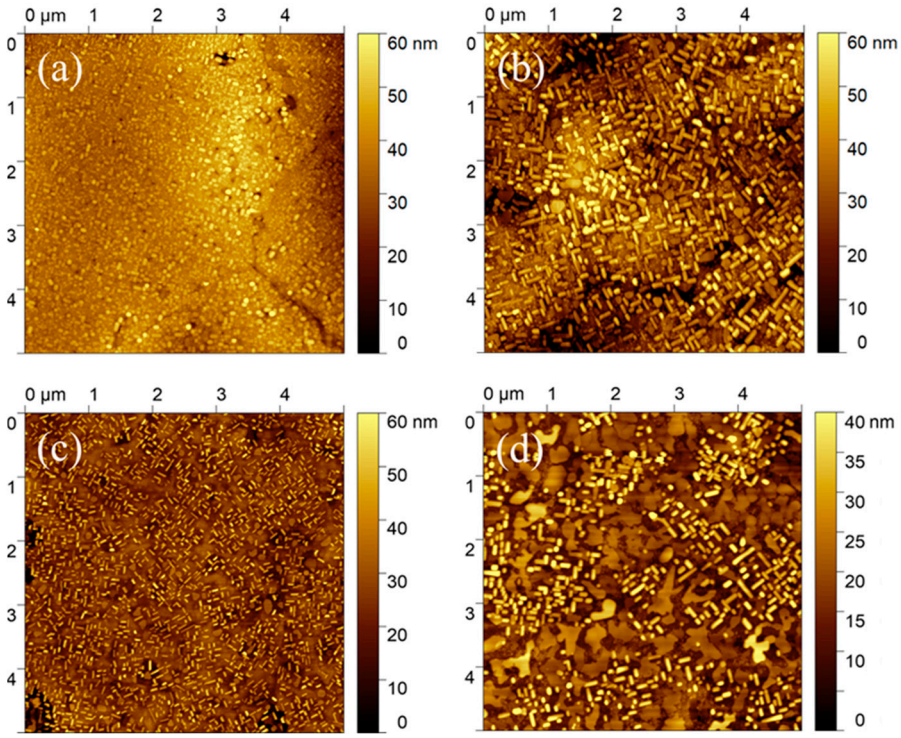

Figure 7. AFM images of PEPI-1 films acquired via XE-100 Park system in true non-contact mode using a ppp-NCHR tip by Nanosensors^{TM}. Images are described as films with different thicknesses: 400 nm (**a**), 90 nm (**b**), 40 nm (**c**), and 12 nm (**d**).

4. Conclusions

In this work, we investigated the crystal growth of Ruddlesden–Popper lead halide perovskite series $(PEA)_2(MA)_{n-1}Pb_nI_{3n+1}$ (n = 1, 2, 3) with the aim of establishing a reliable platform for the realization of phototransistors based on hybrid heterostructures. Good quality crystals were obtained by slow or fast cooling solution methods, as confirmed by X-ray diffraction and confocal micro-photoluminescence analysis. We tested Scotch tape micromechanical cleavage methods and the spin coating technique for realizing ultra-thin layers for hybrid heterostructures, which require large ultra-thin flakes or ultra-thin films.

PEPI-1 crystals were successfully used to obtain few-layer thick flakes by applying the mechanical exfoliation technique, while spin coating was used to achieve thin and ultra-thin films, controlling thickness and morphology. The creation of thin films of PEPI-2 and PEPI-3 compounds remains a challenging task because, as suggested by the crystal

synthesis process, the transition from PEPI-2 to PEPI-3 formation is simply influenced by the cooling temperature gradient of the solution.

Mechanical exfoliation has proven to be the best way to achieve ultra-thin samples. Alternatively, vapor phase processes (PVD or CVD) could be a more versatile dry method for thin and ultra-thin film deposition. As a wet method, spin coating is an easy and well-established method, but for compounds with $n > 1$, it could be useful to focus on other techniques such as blade coating or micro-molding.

Supplementary Materials: The following supporting information can be downloaded at: https://www.mdpi.com/article/10.3390/cryst15121024/s1, Figure S1: Photoluminescence (PL) emission spectra of Ruddlesden–Popper perovskite crystals with n = 2 with the presence of an emission peak at 730 nm maybe related to a High Member Ruddlesden–Popper (HM-RP). The red line is reference for the emission wavelength of MAPI; Figure S2: XRD (a,b) and absorption spectra (c) of films deposited by spin coating on glass substrates using a solution in DMF (0.2 mol/L) obtained dissolving the salts PbI_2: CH_3NH_3I: $C_8H_9NH_3I$ in a stoichiometric ratio of 3:2:2 to obtain n = 3 e.g., $(C_6H_5C_2H_4)_2(CH_3NH_3)_2Pb_3I_{10}$). In (a) we used to heating the solution at 100° and applying post-annealing procedure. In (b) we used only post-annealing procedure. For all the films, we use the following spin coating parameters: spin speet 3000 rpm, spin time 60 s, acceleration 1500 rad/s^2; Figure S3: Graph of the film thickness of PEPI-1 measured by AFM at different molar concentration. A linear behavior is observed; the red line is a linear fit of the data, fit parameters table is reported in the inset.

Author Contributions: Conceptualization, F.C. (Fabio Chiarella); Methodology, F.C. (Fabio Chiarella), G.M.D.L. and F.G.; Validation, F.C. (Fabio Chiarella) and G.M.D.L.; Formal analysis, F.C. (Fabrizio Ciccarelli) and A.C.; Investigation, F.C. (Fabrizio Ciccarelli) and M.B.; Resources, F.C. (Fabio Chiarella) and F.G.; Data curation, F.C. (Fabrizio Ciccarelli), A.C. and F.G.; Writing—original draft, F.C. (Fabrizio Ciccarelli); Writing—review & editing, F.C. (Fabio Chiarella), M.B. and G.M.D.L.; Supervision, F.C. (Fabio Chiarella), M.B. and A.C.; Funding acquisition, F.C. (Fabio Chiarella) and F.G. All authors have read and agreed to the published version of the manuscript.

Funding: This research was funded by Italian Ministry of University and Research (MUR), under the project "Photo-physics and optoelectronics with TMD/2D Perovskite heterostructures for efficient near-infrared detection" PRIN 2022SPCM9R.

Data Availability Statement: The original contributions presented in this study are included in the article/Supplementary Materials. Further inquiries can be directed to the corresponding authors.

Conflicts of Interest: The authors declare no conflicts of interest.

References

1. Chiarella, F.; Zappettini, A.; Licci, F.; Borriello, I.; Cantele, G.; Ninno, D.; Cassinese, A.; Vaglio, R. Combined experimental and theoretical investigation of optical, structural, and electronic properties of $CH_3NH_3SnX_3$ thin films (X = Cl,Br). *Phys. Rev. B* **2008**, *77*, 045129. [CrossRef]
2. Guo, J.; Wang, B.; Lu, D.; Wang, T.; Liu, T.; Wang, R.; Dong, X.; Zhou, T.; Zheng, N.; Fu, Q.; et al. Ultralong carrier lifetime exceeding 20 μs in lead halide perovskite film enable efficient solar cells. *Adv. Mater.* **2023**, *35*, 2212126. [CrossRef]
3. Kim, J.Y.; Lee, J.-W.; Jung, H.S.; Shin, H.; Park, N.-G. High-Efficiency Perovskite Solar Cells. *Chem. Rev.* **2020**, *120*, 7867–7918. [CrossRef] [PubMed]
4. Zhu, H.; Reo, Y.; Park, G.; Yang, W.; Liu, A.; Noh, Y.-Y. Fabrication of high-performance tin halide perovskite thin-film transistors via chemical solution-based composition engineering. *Nat. Protoc.* **2025**, *20*, 1915–1929. [CrossRef] [PubMed]
5. Shooshtari, M.; Kim, S.-Y.; Pahlavan, S.; Rivera-Sierra, G.; Jiménez Través, M.; Serrano-Gotarredona, T.; Bisquert, J.; Linares-Barranco, B. Advancing Logic Circuits with Halide Perovskite Memristors for Next-Generation Digital Systems. *SmartMat* **2025**, *6*, e70032. [CrossRef]
6. Xie, C.; Liu, C.-K.; Loi, H.-L.; Yan, F. Perovskite-Based Phototransistors and Hybrid Photodetectors. *Adv. Funct. Mater.* **2020**, *30*, 1903907. [CrossRef]

7. Ji, K.; Anaya, M.; Abfalterer, A.; Stranks, S.D. Halide Perovskite Light-Emitting Diode Technologies. *Adv. Opt. Mater.* **2021**, *9*, 2002128. [CrossRef]
8. Alvarado-Leaños, A.L.; Cortecchia, D.; Saggau, C.N.; Martani, S.; Folpini, G.; Feltri, E.; Albaqami, M.D.; Ma, L.; Petrozza, A. Lasing in Two-Dimensional Tin Perovskites. *ACS Nano* **2022**, *16*, 20671–20679. [CrossRef]
9. Lee, M.M.; Teuscher, J.; Miyasaka, T.; Murakami, T.N.; Snaith, H.J. Efficient Hybrid Solar Cells Based on Meso-Superstructured Organometal Halide Perovskites. *Science* **2012**, *338*, 643–647. [CrossRef]
10. Mitzi, D.B. *Progress in Inorganic Chemistry*; Karlin, K.D., Ed.; Wiley: New York, NY, USA, 1999; Volume 48.
11. Chakraborty, R.; Paul, G.; Pal, A.J. Quantum Confinement and Dielectric Deconfinement in Quasi-Two-Dimensional Perovskites: Their Roles in Light-Emitting Diodes. *Phys. Rev. Appl.* **2022**, *17*, 054045. [CrossRef]
12. Yaffe, O.; Chernikov, A.; Norman, Z.M.; Zhong, Y.; Velauthapillai, A.; van der Zande, A.; Owen, J.S.; Heinz, T.F. Excitons in ultrathin organic-inorganic perovskite crystals. *Phys. Rev. B* **2015**, *92*, 045414. [CrossRef]
13. Seitz, M.; Magdaleno, A.J.; Alcázar-Cano, N.; Meléndez, M.; Lubbers, T.J.; Walraven, S.W.; Pakdel, S.; Prada, E.; Delgado-Buscalioni, R.; Prins, F. Exciton diffusion in two-dimensional metal-halide perovskites. *Nat. Commun.* **2020**, *11*, 2035. [CrossRef]
14. Mao, L.; Stoumpos, C.C.; Kanatzidis, M.G. Two-Dimensional Hybrid Halide Perovskites: Principles and Promises. *J. Am. Chem. Soc.* **2019**, *141*, 1171–1190. [CrossRef]
15. Yan, J.; Li, H.; Aladamasy, M.H.; Frasca, C.; Abate, A.; Zhao, K.; Hu, Y. Advances in the Synthesis of Halide Perovskite Single Crystals for Optoelectronic Applications. *Chem. Mater.* **2023**, *35*, 2683–2712. [CrossRef]
16. Fateev, S.A.; Petrov, A.A.; Ordinartsev, A.A.; Grishko, A.Y.; Goodilin, E.A.; Tarasov, A.B. Universal strategy of 3D and 2D hybrid perovskites single crystal growth via in situ solvent conversion. *Chem. Mater.* **2020**, *32*, 9805–9812. [CrossRef]
17. Yan, Y.; Yang, Y.; Liang, M.; Abdellah, M.; Pullerits, T.; Zheng, K.; Liang, Z. Implementing an intermittent spin-coating strategy to enable bottom-up crystallization in layered halide perovskites. *Nat. Commun.* **2021**, *12*, 6603. [CrossRef]
18. Muddam, R.S.; Wang, S.; Raj, N.P.M.J.; Wang, Q.; Wijesinghe, P.; Payne, J.; Dyer, M.S.; Bowen, C.; Jagadamma, L.K. Self-Poled Halide Perovskite Ruddlesden-Popper Ferroelectric-Photovoltaic Semiconductor Thin Films and Their Energy Harvesting Properties. *Adv. Funct. Mater.* **2025**, *35*, 2425192. [CrossRef]
19. La-Placa, M.G.; Gil-Escrig, L.; Guo, D.; Palazon, F.; Savenije, T.J.; Sessolo, M.; Bolink, H.J. Vacuum-Deposited 2D/3D Perovskite Heterojunctions. *ACS Energy Lett.* **2019**, *4*, 2893–2901. [CrossRef]
20. Dewi, H.A.; White, L.R.W.; De Luca, D.; Ahmad, R.; Bruno, A. Thermally Evaporated Metal Halide Perovskites for Optoelectronics. *ACS Appl. En. Mater.* **2025**, *8*, 7769–7779. [CrossRef]
21. Chiarella, F.; Ferro, P.; Licci, F.; Barra, M.; Biasiucci, M.; Cassinese, A.; Vaglio, R. Preparation and transport properties of hybrid organic–inorganic CH3NH3SnBr3 films. *Appl. Phys. A* **2007**, *86*, 89–93. [CrossRef]
22. Li, Z.; Hong, E.; Zhang, X.; Deng, M.; Fang, X. Perovskite-Type 2D Materials for High-Performance Photodetectors. *J. Phys. Chem. Lett.* **2022**, *13*, 1215–1225. [CrossRef]
23. Li, J.; Wang, J.; Zhang, Y.; Wang, H.; Lin, G.; Xiong, X.; Zhou, W.; Luo, H.; Li, D. Fabrication of single phase 2D homologous perovskite microplates by mechanical exfoliation. *2D Mater.* **2018**, *5*, 021001. [CrossRef]
24. Fu, Q.; Wang, X.; Liu, F.; Dong, Y.; Liu, Z.; Zheng, S.; Chaturvedi, A.; Zhou, J.; Hu, P.; Zhu, Z.; et al. Ultrathin Ruddlesden–Popper Perovskite Heterojunction for Sensitive Photodetection. *Small* **2019**, *15*, 1902890. [CrossRef]
25. Li, W.; Wang, Z.; Deschler, F.; Gao, S.; Friend, R.H.; Cheetham, A.K. Chemically diverse and multifunctional hybrid organic–inorganic perovskites. *Nat. Rev. Mater.* **2017**, *2*, 16099. [CrossRef]
26. Chen, Y.; Liu, Z.; Li, J.; Cheng, X.; Ma, J.; Wang, H.; Li, D. Robust Interlayer Coupling in Two-Dimensional Perovskite/Monolayer Transition Metal Dichalcogenide Heterostructures. *ACS Nano* **2020**, *14*, 10258–10264. [CrossRef]
27. Yang, A.; Blancon, J.C.; Jiang, W.; Zhang, H.; Wong, J.; Yan, E.; Lin, Y.R.; Crochet, J.; Kanatzidis, M.G.; Jariwala, D.; et al. Giant Enhancement of Photoluminescence Emission in WS2-Two-Dimensional Perovskite Heterostructures. *Nano Lett.* **2019**, *19*, 4852–4860. [CrossRef]
28. Wang, Q.; Zhang, Q.; Luo, X.; Wang, J.; Zhu, R.; Liang, Q.; Zhang, L.; Yong, J.Z.; Yu Wong, C.P.; Eda, G.; et al. Optoelectronic Properties of a van der Waals WS_2 Monolayer/2D Perovskite Vertical Heterostructure. *ACS Appl. Mater. Interfaces* **2020**, *12*, 45235–45242. [CrossRef]
29. Yang, T.; Wang, X.; Zheng, B.; Qi, Z.; Ma, C.; Fu, Y.; Fu, Y.; Hautzinger, M.P.; Jiang, Y.; Li, Z.; et al. Ultrahigh-Performance Optoelectronics Demonstrated in Ultrathin Perovskite-Based Vertical Semiconductor Heterostructures. *ACS Nano* **2019**, *13*, 7996–8003. [CrossRef]
30. Zhou, H.; Lai, H.; Sun, X.; Zhang, N.; Wang, Y.; Liu, P.; Zhou, Y.; Xie, W. Van der Waals MoS_2/Two-Dimensional Perovskite Heterostructure for Sensitive and Ultrafast Sub-Band-Gap Photodetection. *ACS Appl. Mater. Interfaces* **2022**, *14*, 3356–3362. [CrossRef]
31. Peng, W.; Yin, J.; Ho, K.-T.; Ouellette, O.; De Bastiani, M.; Murali, B.; El Tall, O.; Shen, C.; Miao, X.; Pan, J.; et al. Ultralow Self-Doping in Two-dimensional Hybrid Perovskite Single Crystals. *Nano Lett.* **2017**, *17*, 4759–4767. [CrossRef] [PubMed]

32. Du, K.-Z.; Tu, Q.; Zhang, X.; Han, Q.; Liu, J.; Zauscher, S.; Mitzi, D.B. Two-Dimensional Lead(II) Halide-Based Hybrid Perovskites Templated by Acene Alkylamines: Crystal Structures, Optical Properties, and Piezoelectricity. *Inorg. Chem.* **2017**, *56*, 9291–9302. [CrossRef]
33. Bonadio, A.; Sabino, F.P.; Freitas, A.L.M.; Felez, M.R.; Dalpian, G.M.; Souza, J.A. Comparing the Cubic and Tetragonal Phases of $MAPbI_3$ at Room Temperature. *Inorg. Chem.* **2023**, *62*, 7533–7544. [CrossRef]
34. Gesuele, F.; Nivas, J.J.; Fittipaldi, R.; Altucci, C.; Bruzzese, R.; Maddalena, P.; Amoruso, S. Analysis of Nascent Silicon Phase-Change Gratings Induced by Femtosecond Laser Irradiation in Vacuum. *Sci. Rep.* **2018**, *8*, 12498. [CrossRef]
35. Rahil, M.; Ansari, R.M.; Prakash, C.; Islam, S.S.; Dixit, A.; Ahmad, S. Ruddlesden–Popper 2D Perovskites of Type $(C_6H_9C_2H_4NH_3)_2(CH_3NH_3)_{n-1}Pb_nI_{3n+1}$ (n = 1–4) for Optoelectronic Applications. *Sci. Rep.* **2022**, *12*, 2176. [CrossRef]
36. Smith, M.D.; Connor, B.A.; Karunadasa, H.I. Tuning the Luminescence of Layered Halide Perovskites. *Chem. Rev.* **2019**, *119*, 3104–3139. [CrossRef]
37. Stoumpos, C.C.; Soe, C.M.M.; Tsai, H.; Nie, W.; Blancon, J.-C.; Cao, D.H.; Liu, F.; Traoré, B.; Katan, C.; Even, J.; et al. High Members of the 2D Ruddlesden-Popper Halide Perovskites: Synthesis, Optical Properties, and Solar Cells of $(CH_3(CH_2)_3NH_3)_2(CH_3NH_3)_4Pb_5I_{16}$. *Chem* **2017**, *2*, 427–440. [CrossRef]
38. Splendiani, A.; Sun, L.; Zhang, Y.; Li, T.; Kim, J.; Chim, C.Y.; Galli, G.; Wang, F. Emerging Photoluminescence in Monolayer MoS2. *Nano Lett.* **2010**, *10*, 1271–1275. [CrossRef] [PubMed]
39. Niu, W.; Eiden, A.; Prakash, G.V.; Baumberg, J.J. Exfoliation of self-assembled 2D organic inorganic perovskite semiconductors. *Appl. Phys. Lett.* **2014**, *104*, 171111. [CrossRef]
40. Wang, L.; Liu, G.; Xi, X.; Yang, G.; Hu, L.; Zhu, B.; He, Y.; Liu, Y.; Qian, H.; Zhang, S.; et al. Annealing Engineering in the Growth of Perovskite Grain. *Crystals* **2022**, *12*, 894. [CrossRef]
41. Abdelhamied, M.M.; Song, Y.; Liu, W.; Li, X.; Long, H.; Wang, K.; Wang, B.; Lu, P. Improved photoemission and stability of 2D organic-inorganic lead iodide perovskite films by polymer passivation. *Nanotechnology* **2020**, *31*, 42LT01. [CrossRef]
42. Mallik, K.; Dhami, T.S. Optical absorption spectra of lead iodide nanoclusters. *Phys. Rev. B* **1998**, *58*, 13055–13059. [CrossRef]